



Research Article

Green synthesis of Cu/Cu₂O/CuO nanostructures and the analysis of their electrochemical properties

Xolile Fuku¹  · Mmalewane Modibedi¹ · Mkhulu Mathe¹

Received: 30 December 2019 / Accepted: 6 April 2020 / Published online: 15 April 2020
© Springer Nature Switzerland AG 2020

Abstract

Heterogeneous Cu/Cu₂O/CuO nanoparticles were synthesised via polyphenols of pomegranate for various application. X-ray diffraction and high resolution-scanning electron microscopy confirmed Cu/Cu₂O/CuO NPs crystallinity and the particle size which ranged from 5 to 20 nm. The electrochemical band gap energies of Cu/Cu₂O/CuO NPs were calculated to be between 0.9 and 2.1 eV. EIS measurements were used to calculate the capacitance and specific capacitance of the nanoparticles which were found to be 11.2 F and 69 F g⁻¹. Surface diffusion coefficient obtained from cyclic voltammetry was found to be $1.54 \times 10^{-6} \text{ cm}^2 \text{ s}^{-1}$ with r^2 of 0.99 suggesting a fast electron movement. The calculated surface coverage was $1.38 \times 10^{-3} \text{ mol cm}^{-2}$ suggesting the formation of monolayer at the electrode interface. The results confirmed the electroactivity of Cu/Cu₂O/CuO electrode towards the volatile organic compound- ethanol. Cu/Cu₂O/CuO exhibited good electrochemical performance towards ethanol with higher current density and most negative onset potential -0.3 V, meaning that it requires lower energy for ethanol activity to occur at the electrode interface. EIS profiles confirmed the kinetics of Cu/Cu₂O/CuO at the electrode surface with characteristic small circular curvature signifying that the polarisation resistance (R_p) is prominent, proposing a faster electron shuttling process for ethanol activity. Further, the amperometric response with long time test for the Cu/Cu₂O/CuO based electrode system estimated a lower limit of detection to be 0.09 μM at a signal to noise ratio of 3 with sensitivity of 0.049 $\mu\text{A } \mu\text{M}^{-1}$ at steady state. Raman and FTIR highlighted mechanism of coordination.

Keywords Cu/Cu₂O/CuO nanoparticles · Pomegranate · Electrochemical methods · Ethanol activity · Capacitance · Mechanism

1 Introduction

Of late, Green synthesis has become a centre of attention in different disciplines of nanotechnology. The term 'Green chemistry' was invented by the US Environmental Protection Agency (EPA-1990s) with the aim to stimulate cutting-edge eco-friendly technologies in the production, design and use of chemical products [1–3]. In the last decade, Green Chemistry was used to achieve sustainability since it was adopted as a culture and a methodology. Current developments in nanotechnology, particularly the

capability to synthesise highly methodical nanomaterials of any shape and size, have led to the production of innovative materials. The characters of metal and metal oxide nanomaterials have been of great interest due to their distinctive feature such as catalytic activity, optical, magnetic and electrical properties [4–9]. Nanoparticles coordination with biological entities (e.g., microorganisms) has created a succession of nanoparticle-biological interfaces that depend on both colloidal forces and dynamic biophysicochemical interactions [2, 5, 6]. During coordination, new nanomaterials with controlled morphology, surface

✉ Xolile Fuku, xfuku@csir.co.za; Mmalewane Modibedi, mmodibedi@csir.co.za | ¹CSIR Energy Centre, PO Box 395, Pretoria 0001, Republic of South Africa.



chemistry, roughness and surface coatings are formed. Use of plants as a protocol for nanoparticle synthesis provides a cost-effective and eco-friendly alternative to chemical and physical synthesis [6, 10, 11]. Relative to their counterparts, plants can be scaled up for large-scale synthesis without employing harsh chemicals and the demand for high energy, temperature and pressure. Further, this substantiate that the green method of synthesis is easy, efficient, and eco-friendly relative to chemically mediated synthesis [12–14]. Though not much has been done, scientists have engaged themselves in the green production of different metal oxide NPs for various applications. Raja Naika et al. [15] prepared bio-inspired Cu/Cu₂O/CuO nanoparticles and reported their antibacterial activity. Other oxide NPs (TiO, NiO, MgO etc.,) have been synthesised using different plants such as neem [15], alfalfa [15], cinnamomum camphora, emblica officinalis, lemon grass, tamarind, and euphorbia tirucalli [16, 17] for applications such as solar systems, supercapacitors etc.,. Due to their technological applications in the fields such as sensors, conductors, catalysis, energy [18, 19], transformation and preparation of organic–inorganic nanostructure composites [18, 20–22] Cu, Cu₂O or CuO and Cu–Cu₂O–CuO NPs have attracted significant attention in the research community [23–25]. Copper oxides (Cu₂O or CuO) are among the important oxide materials because of their versatile functionalities and their low cost and toxicity are advantageous for commercial uses [24–26]. Key applications of Cu₂O or CuO in chemistry include catalysis, solar cells, batteries, and, gas sensors [27]. For such applications, Cu₂O or CuO nanostructures such as nanoparticles, nanocrystals, nanorods, nanocubes, nanosheets, etc. have been used extensively to enhance catalytic performance [24–26, 28]. These nanomaterials reveals mixed phase properties and are regarded as p-type and monoclinic crystal structure with indirect and direct band gap band gap energies ranging between ~ 1.4 and 2.8 eV [29–32]. Furthermore, when integrated in coatings and textiles the metal oxides can be used as an anti-fungal agent, antimicrobial, anti-biotic [19]. Different methods such as sonochemical, alkoxide based route, electrochemical methods, precipitation-pyrolysis, microwave irradiations, [33–35] and thermal decomposition of precursor [19, 33–36] have been used to synthesise Cu/Cu₂O/CuO NPs. Nonetheless, these synthetic routes are prone to toxicity and other drawbacks in many application fields (e.g., medical application). Recently, green syntheses of different nanoparticles by plants have been reported [4, 36]. For this view, we present an undemanding and eco-friendly biosynthesis of Cu/Cu₂O/CuO nanoparticles using pomegranate peel extract and highlight their electrochemical and catalytic activity towards ethanol. Furthermore, the pomegranate method of synthesis required no harsh chemicals, no prolonged periods and no high

energy requirements for preparing Cu/Cu₂O/CuO NPs, thus proving to be an innovative method.

2 Experimental procedures

2.1 Reagents and materials

Copper chloride salt (CuCl, 99.98%) and Silver/Silver chloride (Ag/AgCl, 3 M), Polyesterine graduated tubes and 0.22 μm hydrophilic filters (Whatman) were used for NPs preparation. Phosphate buffer solution (PBs), 0.1 M, pH 7.0 was prepared from anhydrous potassium hydrogen phosphate (Na₂HPO₄) and potassium dihydrogen phosphate (NaH₂PO₄) while purified deionized water was used for aqueous solution preparations as recorded in our previous study [37]. Pomegranate fruits were purchased from vendors. All chemicals were supplied by Sigma-Aldrich.

2.2 Synthesis of reduced Cu/Cu₂O/CuO nanoparticles from pomegranate peel extract

Dried Peels of pomegranate (40 g) were added into a 250 mL conical flask of deionised water (40 °C, 1 h), a yellow to reddish brown extract was formed with a recorded solution pH = 3. The broth/extract was filtered with Whatman paper (0.22 μm). 8 g of the copper chloride salt was then dissolved in 200 mL of pomegranate broth and the aliquot was subjected to a constant temperature (80 °C), after which a dark green–brown precipitate of copper/cupric oxide (Cu/Cu₂O/CuO) nanoparticles (NPs) (pH 5) was formed. For microscopic (SEM) and spectroscopic (XRD) analysis, the precipitate was collected via centrifugation (10 min, 1000 rpm) and the nanomaterials washed with deionized H₂O three times in order to remove loosely bound materials, using a centrifuge and a sonicator [38]. 80% yield of the nanopowder was realised and was oven dried at 65 °C, 30 min. The as-prepared Cu/Cu₂O/CuO nanoparticles were then crushed into a powder using mortar and pestle, after which the nanomaterials were calcinated at different temperature (100 °C, 200 °C, 300 °C, 400 °C and 500 °C). The Cu/Cu₂O/CuO nanoparticles were re-dispersion (20 min) in 0.1 M phosphate buffer (pH 7.0) for further analyses.

2.3 Preparation of GC/Cu/Cu₂O/CuO electrodes

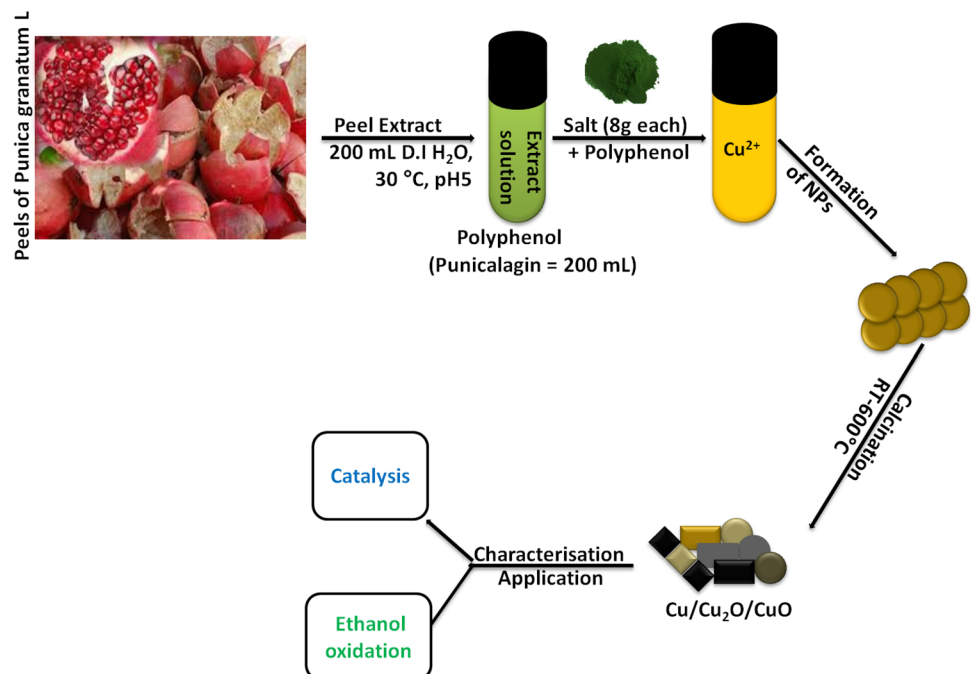
Glassy carbon electrode (GCE) was thoroughly cleaned by sonication in absolute ethanol and deionized water (5 min), respectively and finally rinsed with distilled water. The electrode (GCE) was drop-coated with Cu/Cu₂O/CuO NPs solution (60 μL), dried at 50 °C for 15 min, and followed by gently washing with distilled water to remove unbound

particles. The electrode was labelled as GC/Cu/Cu₂O/CuO. For electrochemical measurements Phosphate buffer solution (0.1 M, pH 7) was employed as the electrolyte as was noted from previous our study [38] (Scheme 1).

2.4 Instrumentation and electrochemical measurement

Surface morphology and particle size dispersion of the prepared Cu/Cu₂O/CuO nanoparticles were examined using high resolution electron microscope (TEM, JEOL 2011). Electron dispersion spectroscopy (EDS) together with X-ray diffraction (XRD- Rigaku D/MAX-PC 2500 X-ray diffractometer with a CuK_α ($\lambda = 1.54 \text{ \AA}$) at 40 kV and 200 mA) were used to enabled components of the as prepared nanomaterials. Transmittance (%T) and vibrational/absorption bands were determined using Infrared Spectroscopy (FTIR on a Perkin Elmer spectrometer Spectrum 100). Emission and wavelength bands were determined by employing Fluorescence-fibre optic ocean-view LEDs and UV/Vis absorption spectroscopy using fibre optic ocean-view detector. Raman spectra were obtained on Horiba scientific, Olympus Model No BX41TF MAT 200 kV. Electrochemical experiments such as, cyclic voltammetry (CV) and electrochemical impedance spectroscopy (EIS) were performed using an Autolab potentiostat, Metrohm. A typical three-electrode system made of auxiliary (Ag/AgCl reference) electrode, a platinum wire-counter electrode and a glassy carbon (GCE) working electrode were used in all electrochemical measurements with 0.1 M PBS (pH 7) used as an electrolyte [38].

Scheme 1 Schematic representation of Cu/Cu₂O/CuO NPs synthesis and its characterisation



3 Results and discussion

3.1 Optical properties of Cu/Cu₂O/CuO NPs

Figure 1a shows the UV-visible absorption spectra of colloidal Cu/Cu₂O/CuO nanoparticles with average nanoparticle sizes of 5–20 nm. The figure further illustrates the temperature dependence process of the as-prepared nanoparticles. Compared to the control (insert: peel extract at $\lambda_{\text{max}} = 374 \text{ nm}$), Fig. 1 depicts absorption peaks at about 206, 306, 546 and 830 nm for all five samples (25–500 °C), respectively. The peaks at 206 and 306 nm corresponds to inter band transition from deep level electrons of valance band of Cu/Cu₂O while the peak around 380 nm is due to the band edge transition of CuO/Cu₂O [38–40]. The peaks at 546 and 830 nm are attributed to existence of Cu/Cu₂O/CuO on the surface of the synthesized material [39, 41, 45, 46]. The obtained results are comparable with literature [30, 39, 42, 43]. The results suggest that Cu/Cu₂O/CuO NPs were formed after interaction with the biomolecules, apparent by a shift in λ_{max} . From the observed spectra, a decrease in peak intensities (from low to higher temperatures) is evident with slight shifts in absorption maxima. However, at high calcination temperatures Cu/Cu₂O/CuO particles exhibits relatively lower absorptions intensities [43, 44]. The shifts and low absorptions in electronic and optical properties can be viewed as a function of NPs size and shape. In addition, due to the transformation of the random nanoparticle shapes to nearly spherical and the increase

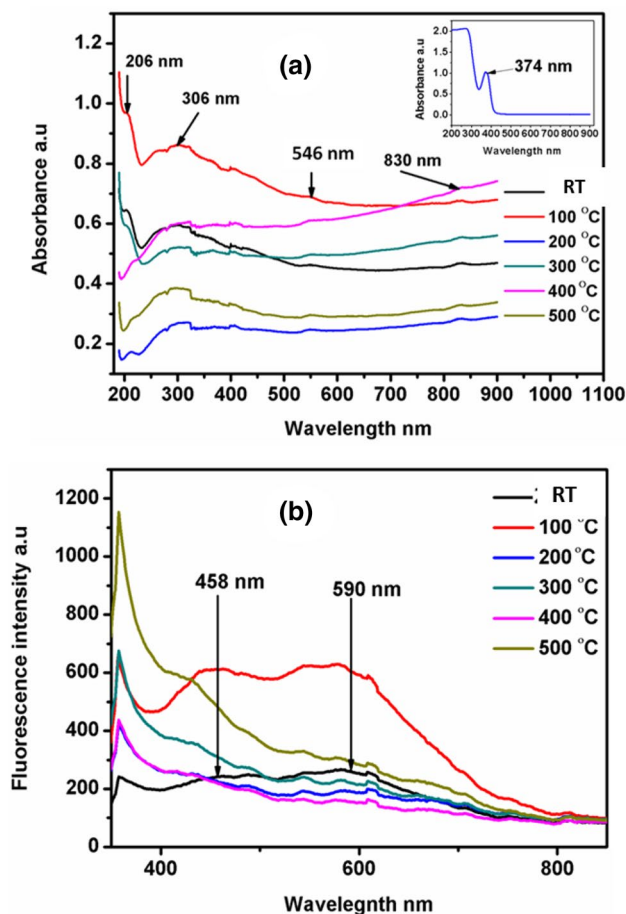


Fig. 1 UV-vis spectra (a) and (b) PL spectra of Cu/Cu₂O/CuO NPs at different annealing temperatures

of the average particle size, the sp resonance shifts to red and becomes broader showing the inter-diffusion of the metals-ligands thus forming a ternary/alloying NPs. This behavior could also be attributed to the concentration of conduction electrons/intra-band transitions of the energy state.

Figure 1b shows the corresponding fluorescence spectra of Cu/Cu₂O/CuO NPs at different calcination temperatures. A pronounced emission band appeared at 275 nm and is largely attributed to a near-band-edge emission band and another broad band was noted ranging from 458 to 590 nm [44]. According to literature, the green emission band at 590 nm is due to the ionized oxygen vacancies [35, 39]. At around 670 nm emission shifts from green to near yellow due to interstitial in Cu/Cu₂O/CuO NPs were observed and are assigned to surface defects presence, which are expected to be of large density in nanoparticles of small sizes [45, 46]. The visible photoluminescence sparks from the radioactive recombination of an electron occupying the oxygen vacancy with photo-generated hole [41, 47, 48]. Therefore, decreases

in PL intensities are attributed to more photo-induced electrons that are trapped and stably transferred through the interface whilst the enhanced PL spectrum denotes a fast recombination rate of electron-hole pairs. A further comparison study of PL data and the UV-Vis absorption maxima measurements showed that the obtained results are consistent with each other.

3.2 Morphology, structure and functionality of Cu/Cu₂O/CuO

Further evidence of the as-prepared Cu/Cu₂O/CuO NPs formation was provided by HRSEM and HRTEM, Figs. 2 and 3. HRSEM and HRTEM provided the size, morphology and structural properties of the as-synthesised Cu/Cu₂O/CuO NPs. Figure 2a–g shows the HRSEM micrographs of the as-synthesised Cu/Cu₂O/CuO NPs at different annealing temperatures (a: RT, b: 100 °C, c: 200 °C, d: 300 °C, e: 400 °C, f: 500 °C, g: 500 °C).

SEM micrographs (Fig. 2a–g) reveals different Cu/Cu₂O/CuO structures while providing evidence of the Cu/Cu₂O/CuO constituents, Fig. 2h. Figure 2a show agglomerated cube-like, rod-like and spherical like structures of the as-prepared Cu/Cu₂O/CuO nanocomposites while unveiling porous nano-micro structures at higher temperatures (Fig. 2b—100 °C, 2c—200 °C, 2d—300 °C and 2e—400 °C and 2f—500 °C). Meanwhile, Fig. 2f shows combined phases of spherical like structures growing within the nano-micro structures of the prepared Cu/Cu₂O/CuO nanocomposites. Literature provided evidence that the Cu/Cu₂O/CuO mixed phases and nano-micro structures can be used in different applications such as energy and biomedical technology [31, 32]. HRTEM (Fig. 3a–f) was also employed to confirm and elucidate the nature of the as-synthesised NPs. The HRTEM images was able confirm and provide evidence of Cu/Cu₂O/CuO particle size distribution at different temperature (RT–600 °C) and was found to be 2–20 nm. Meanwhile, SEM mapping (Fig. 3g–h) micrographs proved the formation of Cu–Cu–O–Cu₂O showing different positioning of metal-metal oxides. Therefore, SEM and TEM micrographs are in agreement in-terms of change in structure as the temperature moves from low to optimal temperatures.

Raman and FTIR spectra (Fig. 4a, b) were able to provide additional insight into the structure and properties of the prepared Cu/Cu₂O/CuO nanocatalyst. To investigate local atomic arrangement, vibrational modes and crystallinity of Cu/Cu₂O/CuO NPs, Raman spectroscopy (Fig. 4a) was utilized. According to literature [49, 50] CuO NPs belongs to C6_{2h} space group. The $\Gamma_{RA} = 4Au + 5Bu + Ag + 2Bg$ modes which are called zone-centre optical-phonon are reviewed here, where G = vibrational freedom, Au and Bu represent IR modes, Ag and Bg represents Raman modes [51,

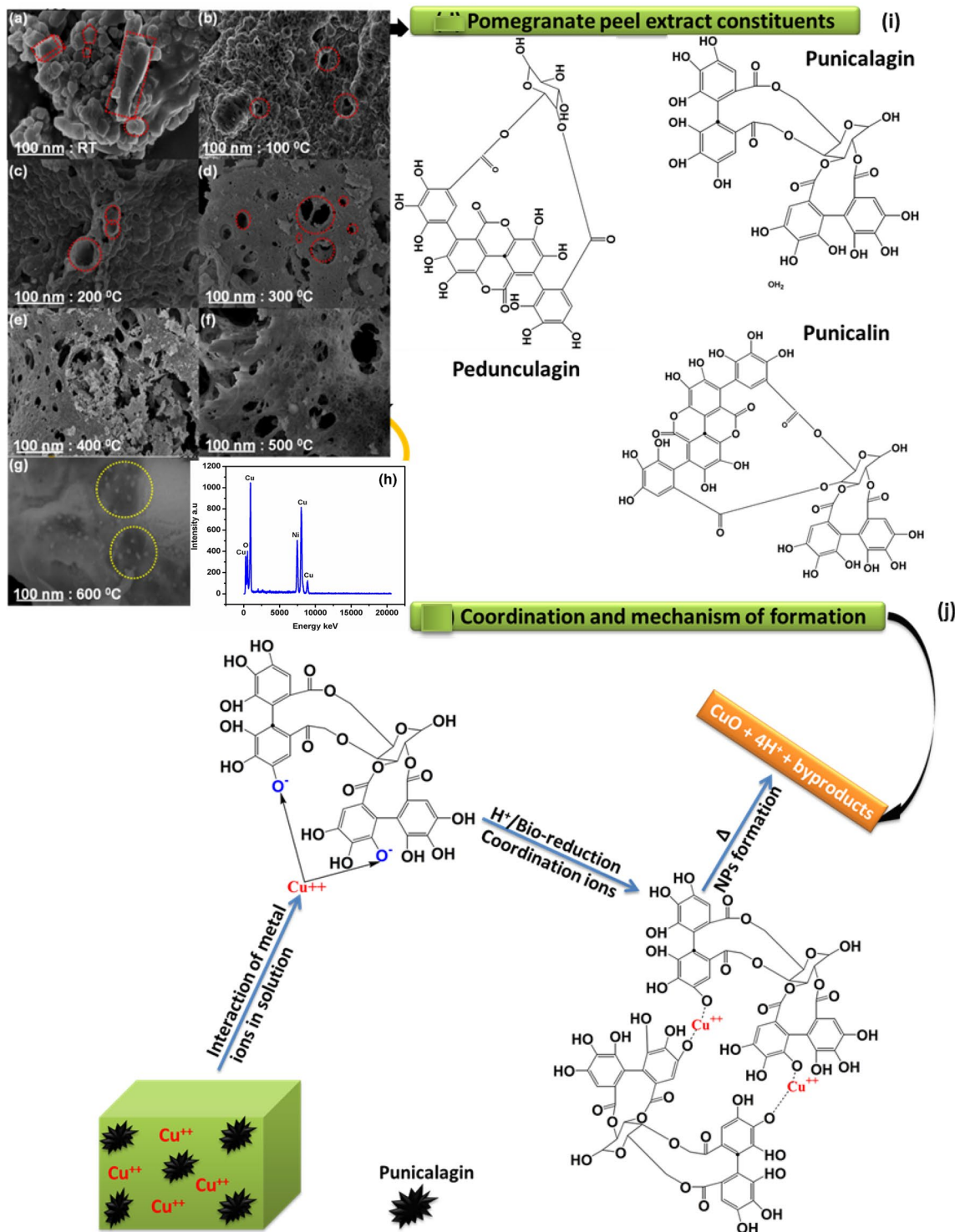


Fig. 2 SEM images of as-prepared Cu/Cu₂O/CuO NPs **a** RT, **b** 100 °C, **c** 200 °C, **d** 300 °C, **e** 400 °C, **f** 500 °C, **g** 600 °C and **h** EDX spectra of the prepared Cu/Cu₂O/CuO NPs

52]. Further, the calculated [53] structural and vibrational properties of cuprite Cu₂O were observed and according to the group theoretical selection rules, the cuprite structure allows only a single Raman-active mode (T2g).

Its frequency is indicated in Fig. 4 and corresponds to the broad feature at $\omega \approx 500\text{--}520\text{ cm}^{-1}$ and this agrees well with literature values [53]. The Cu-Cu₂O and CuO particles exhibited their characteristic Raman bands at

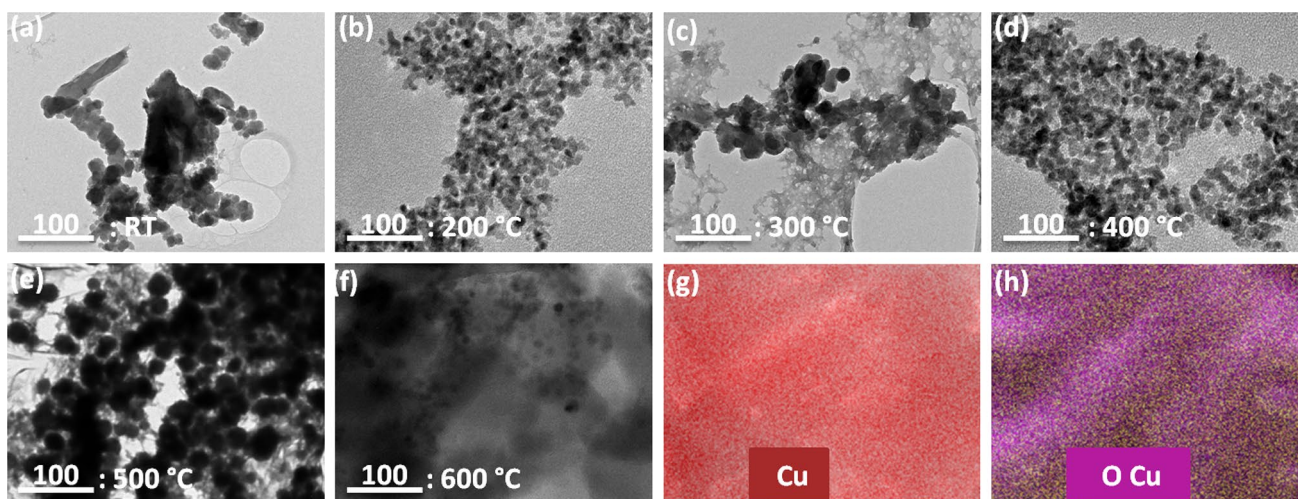


Fig. 3 HRTEM images of as-prepared Cu/Cu₂O/CuO NPs **a** RT, **b** 200 °C, **c** 300 °C, **d** 400 °C, **e** 500 °C, **f** 600 °C and **g, h** EDX mapping spectra of the prepared Cu/Cu₂O/CuO NPs

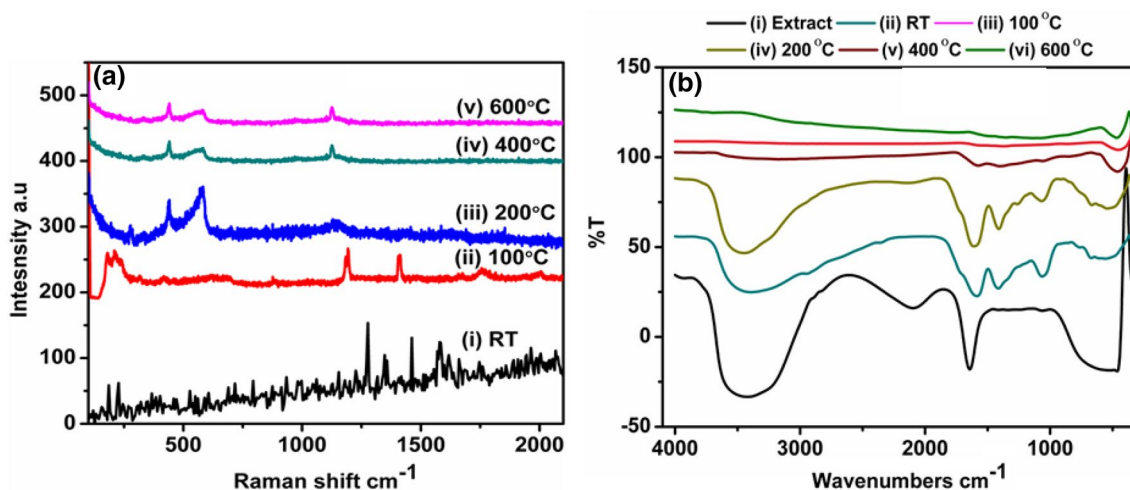


Fig. 4 Raman **(a)** and FTIR **(b)** spectra of as-prepared Cu/Cu₂O/CuO nanocomposites

488 and 523 cm⁻¹. The Raman peaks are broad, the peak at 432 and 574 cm⁻¹ can be attributed to the Bg modes [50–52]. Additional Raman peak was also observed at 1107 cm⁻¹ and corresponds to a multiphonon band of Cu/Cu₂O/CuO nanostructures, relating to the harmonic coupling between phonons [50]. In particular, the multiphonon band 2Bg in Cu/Cu₂O/CuO was suggested to be the stretching vibration in the ²⁻² plane [50]. Figure 4a(i–v) represent the Raman spectra of the synthesised Cu/Cu₂O/CuO NPs at different temperatures. As we move from low to high temperature the structure of the prepared material becomes clearer since all the impurities are removed. The resultant spectra at higher temperature suggest that formation of pure Cu/Cu₂O/CuO requires high energies. The

frequencies of all Raman bands observed in this study are similar to those obtained by other researchers [54].

IR-spectroscopy was utilized to characterize the surface nature of the resulting Cu/Cu₂O/CuO NPs, as depicted in Fig. 4b. Strong band at 512 cm⁻¹ related to the vibrations of the Cu–O functional group was observed (Fig. 4b). This confirmed the presence of nanosized Cu/Cu₂O/CuO particles. The extract which serves as the control in this case (Fig. 4b), show intense and broad band at 3430 cm⁻¹ corresponding to the stretching hydroxyls of adsorbed water [56, 57]. The peak at 1020 cm⁻¹ indicated the presence of C–O stretching frequency of carboxylate ion bond to the Cu/Cu₂O/CuO nanoparticles as bidentate ligand [56, 57], whereas the peak at 1600 cm⁻¹ signified the unreacted

carboxyl group proposing the existence of flavonones adsorbed on the Cu/Cu₂O/CuO NPs surface [58]. The results propose that water soluble organic moieties of peel extract were accountable for the formation and stability of the as-prepared Cu/Cu₂O/CuO NPs. Furthermore, broad vibrational stretches were also observed at 2002 cm⁻¹ and 1433 cm⁻¹ which were mainly attributed to the chemisorbed and physisorbed H₂O and CO₂ molecules on the surface of Cu/Cu₂O/CuO particles [59, 60]. A similar behaviour was also reported by other researchers [59–61]. Compared to the control (peel extract, Fig. 4b), the spectrum at higher temperature confirms the formation of pure Cu/Cu₂O/CuO NPs evident by absence of hydroxyl and carboxylate vibrational stretches.

FTIR and Raman (Fig. 4a, b) spectroscopy were also utilised to reveal the proposed mechanism of coordination as reviewed in our previous study [62, 63]. With few alterations, briefly: CuCl₂ as a precursor separates into ions (Cu⁺⁺) when in solution. Meanwhile, hydroxyl and ketonic groups (from phenolic compounds) contained in the extract were able to interact with metal ions which were reduced and capped to nanosize particles. After interaction and chelation of polyphenols to ions, coordination occurred and a complex-ligand (Cu⁺⁺-polyphenols) was formed through the displayed constituents (Fig. 2i–j). To further support this coordination and mechanism of formation (Fig. 2i–j), a comparison study of the IR and Raman spectra between the synthesised nanoparticles and the solution extract (control) was carried out, Fig. 4a, b. Compared to the control, the nanoparticles showed a reduction in transmission and a shift in wavenumbers at around 3430 cm⁻¹ (OH⁻ absorption), 1600 cm⁻¹ (C=O), and 512 cm⁻¹ proving coordination and formation complex-metal ligand. Though, varying the calcination temperature demonstrated the deformation of the (OH), ν (C=O) and ν (CO) vibrational modes, signifying the formation and deprotonation of the pure Cu/CuO at 512 cm⁻¹ and at 1110 cm⁻¹ is broader vibrational stretch of Cu–O in Cu₂O, thus confirming the formation of Cu/Cu₂O/CuO. Raman and FTIR spectra (Fig. 4a, b) revealed the purity of the prepared nanoparticles, evident by the observed Cu–CuO, Cu₂O phonons. It is evident that the mechanism of the reduced nanoparticles has been established from supporting IR, Raman, TEM and SEM studies by providing details of different phases and structures of the produced mixed phase Cu/Cu₂O/CuO. To further support our proposition, we have prepared a compositionally similar Cu–CuO nanocomposite using Cu⁺⁺ and polyphenols of pomegranate extracts which displayed lower rate of reduction at RT towards the formation of the ternary oxides. However, as we increase the annealing temperature the production of ternary nanocomposite (Cu/Cu₂O/

CuO) become apparent along with the formation of Cu/Cu₂O, Cu/CuO etc. and this was due to the unique aqueous synthetic procedures of the nanoparticles.

3.3 Crystallinity of Cu/Cu₂O/CuO NPs

The crystallographic structures, phase identification and size of the synthesised NPs were determined by XRD-Rigaku (PXRD-7000) using Cu-K α radiation of wavelength $\lambda = 1.541 \text{ \AA}$ and thermal gravimetric analysis (DSC/TGA) Fig. 5. The synthesised nanopowder clearly directs the occurrence of two crystalline phase indices, monoclinic cupric oxide (CuO) and cubic cuprous oxides (Cu₂O) at both low and high temperatures (RT–600 °C), Fig. 5a. The presences of these two phases were also confirmed by UV–Vis and fluorescence results. The (110), (111) and (200) indices planes are assigned to 2θ values of 37°, 42°, and 45° which agree with those of mixed phase powdered Cu₂O, CuO, Cu obtained from JCPDS file number 75-1525 and confirm the creation of Cu/Cu₂O/CuO structure [6, 63], as the temperature is increased (300–500 °C) pure Cu/Cu₂O/CuO NPs become evident. CuO particles peaks which are same as single cubic phase monoclinic (JCPDS: 80-1916) structure with a lattice constant $a = 4.68830 \text{ \AA}$, $b = 3.42290 \text{ \AA}$ and $c = 5.13190 \text{ \AA}$, $\beta = 99.51$ are shown in Fig. 5a. The base-centre monoclinic cupric oxide (Cu–CuO) exhibiting 2θ values 32°, 37°, 42°, 62°, 76° and 78° with phases (110), (111), (200), (220), (311) and (222) matched well JCPDS card number 75-1525 which correspond with the values of tenorite-monoclinic phase CuO and cupric Cu₂O as reported by Volanti et al. [63, 64], Vinod et al. [1], Amrut et al. [5] and recently by Abboud et al. [6]. From the observed results, it can be noted that due to changes in calcination temperature from 400 to 500 °C there is a slight shift towards lower angles. In addition, the observed increase (at 400 °C) and/or decrease (at 500 °C) in peak intensity proves the formation of pure and highly crystalline Cu/Cu₂O/CuO NPs. Due to an increase in temperature, the peak intensity of Cu/Cu₂O/CuO NPs becomes inversely-proportional (increase) to the full width at half maximum (FWHM), illustrating possible alteration in the Cu/Cu₂O/CuO grain size [6, 43] and ensures the formation and enhanced crystallinity of the prepared material. Evidently cupric oxide has high content than cuprous oxide which reveals its higher intensity at 42° and 62° and demonstrating that the varied phase has main proportions of CuO/Cu₂O with the highly oriented crystalline Cu/Cu₂O/CuO phase. The mean particle size of Cu/Cu₂O was calculated from the line broadening of Cu/Cu₂O/CuO [200] peak ($2\theta = 42^\circ$) by Scherrer equation [32, 62].

The mean particle size was calculated using the Scherrer formula (Eq. 1),

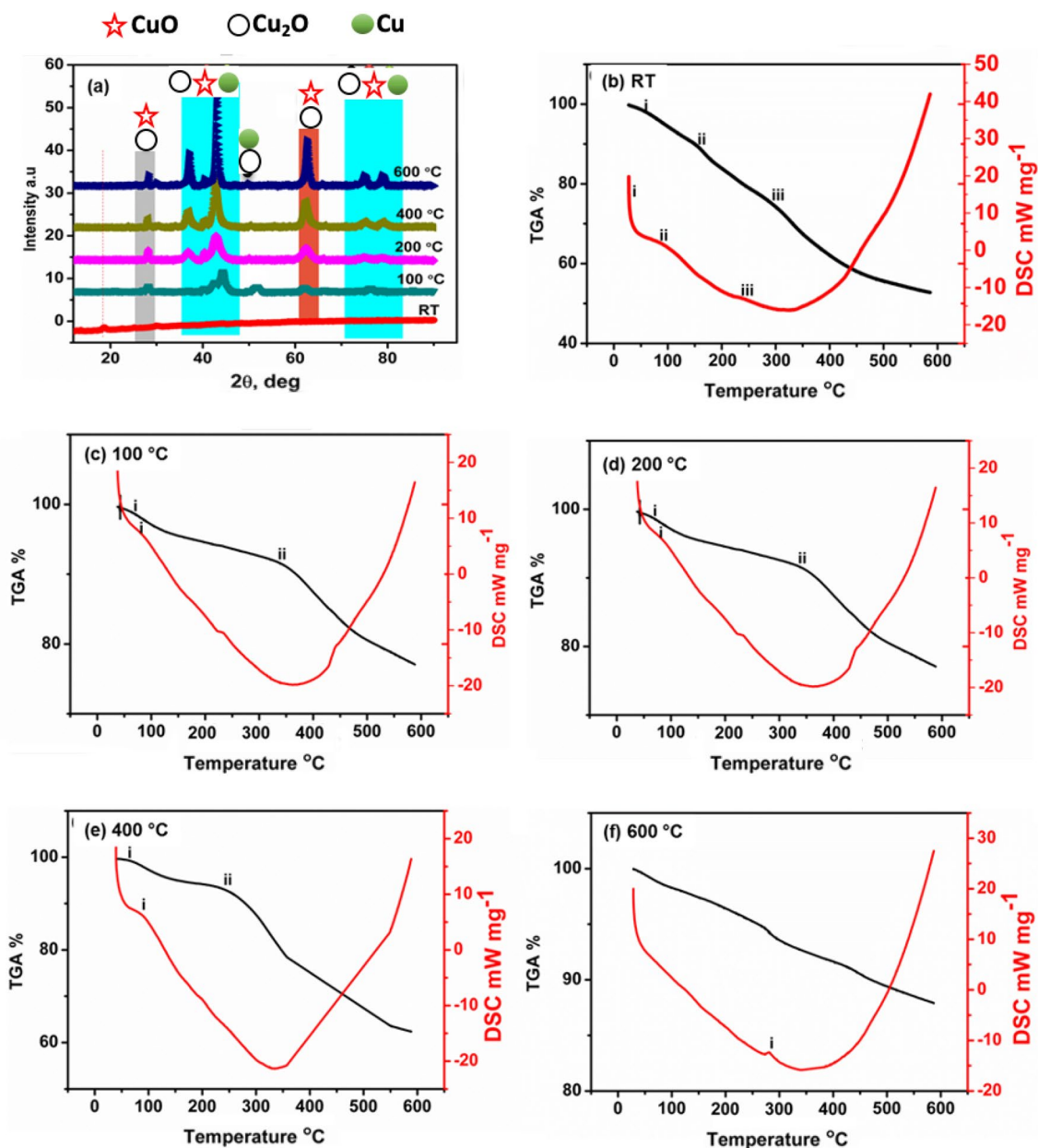


Fig. 5 Thermal analysis of Cu/Cu₂O/CuO nano-composite subjected to different temperatures (RT- 600 °C)

$$D = \frac{k\lambda}{\beta \cos \theta} \tag{1}$$

where *D* is mean particle size, *k* (is a constant) = 0.9, *λ* is wavelength of X-ray source (0.1541 nm), *β* is the FWHM and *θ* is the half diffraction angle. The average particle size was calculated to be 20–25 nm which is comparable with other results [62]. UV–VIS absorption spectra, The XRD pattern, TEM and SEM micrographs, together provides strong evidence for the existence and size of Cu/Cu₂O/CuO NPs [63].

Combined plots of (Fig. 5b–f) at different temperatures (RT, 200 °C, 400 °C, 500 °C and 600 °C) are observed. DSC/TGA analysis of the uncalcined and calcinated Cu/Cu₂O/CuO catalyst was carried out to ascertain the thermal stability of the nano-catalyst. TGA plots confirm weight loss (peak I–III) starting from 100 to 400 °C, Fig. 5b–e). According to the DSC thermograms (Fig. 5b), four exothermic peaks were evident at 90 °C, 250 °C (Fig. 5a–c peaks I–III), 300 °C and 330 °C (Fig. 5e, f peaks I–II), respectively. The decomposition of the sample may be due to the

condensation dehydration of the polyphenols (especially kenotic ($-C=O$) and hydroxyl (OH^-) group) and also from water vapour. Notably, at $600\text{ }^\circ\text{C}$ the TGA curves reveal no weight loss of the nanocatalyst, thus concluding a thermally stable and pure $Cu/Cu_2O/CuO$ nanocomposite. The results are in agreement with our previous FTIR results [38]. The results further confirm that the thermal decomposition of the catalyst is complete below $600\text{ }^\circ\text{C}$.

3.4 Catalytic properties and effect of $Cu/Cu_2O/CuO$ NPs

Cyclic voltammetry was used to investigate the electrochemical behaviour of the synthesised $Cu/Cu_2O/CuO$ NPs. In addition, to also study the band gap energies of the NPs when subjected to different annealing temperatures ($25\text{--}500\text{ }^\circ\text{C}$). Figure 6 shows typical CVs of naked GCE and $Cu/Cu_2O/CuO$ -modified GCE (GCE/ $Cu/Cu_2O/CuO$) in 0.2 M PBs, pH 7.

Compared to modified electrode, the bare GCE electrodes possess no redox properties (Fig. 6a), meanwhile the redox properties of the synthesised $Cu/Cu_2O/CuO$ NPs were revealed at the electrode interface (Fig. 6b). The as-prepared NPs shows two oxidation peak currents ($I_{p,a}$) at oxidation peak potentials ($E_{p,a}$) of -0.4 V and reduction peak potential ($E_{p,c}$) $= -0.01\text{ V}$, respectively (Fig. 6(a) d and a). Small oxidation peak current ($I_{p,a}$) at $E_{p,a} = -0.4\text{ V}$ was observed (Fig. 6(a) d) and has been attributed to the adsorption of oxygen [55], whilst the $I_{p,a}$ at $E_{p,a} = -0.01\text{ V}$ (Fig. 6(a) a) corresponds to the oxidation of Cu_2O to CuO NPs [62, 65]. The cathodic peak current ($I_{p,c}$) at $E_{p,c} = -0.15\text{ V}$ (Fig. 6(a) b) represents the reduction of $[Cu(OH)_2]$ and cathodic peak current (Fig. 6(a) c) at $E = -0.35\text{ V}$ results from the reduction of mixed phase $Cu-Cu_2O/CuO$ [65–67]. The obtained results confirm the formation of the synthesised nanomaterials and are in

good agreement with literature [65–67]. The reported results can be correlated with the following reactions [62, 66]:

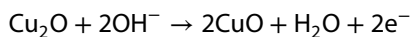
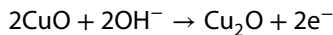


Figure 6b reveals CVs of GCE/ $Cu/Cu_2O/CuO$ in 0.2 M PBs, pH 7.0 at different annealing temperatures. Relative to the RT NPs, a shift in the reduction and oxidation peak potentials was noted. The shift in peak potential was from -0.2 to -0.3 V and -0.01 to -0.04 V (between: 25 and $100\text{ }^\circ\text{C}$) with peak to peak separation of $0.3\text{--}0.5\text{ V}$. In addition, a decrease in peak currents (Fig. 6a–c) was also observed which can be attributed to the formation and shape of the pure crystalline Cu/Cu_2O NPs. Furthermore, as we increase the annealing temperature the oxidation and reduction peak currents at $E = -0.4\text{ V}$ and $E = -0.15\text{ V}$ decreases in intensity to almost disappearing (Fig. 6b, d), confirming the formation of crystalline $Cu/Cu_2O/CuO$ NPs as both the reduction and oxidation peaks of $Cu-CuO/Cu_2O$ NPs remain constant. From Fig. 6, we were able to calculate the band gap energy of the synthesised NPs since it has been established that the potentials related to the cathodic and anodic curves obtained from cyclic voltammetry can be utilised to assess the ionization energy (I_p) and the electron affinity (E_a), as well as the difference between the lowest unoccupied molecular orbital (LUMO) and the highest occupied molecular orbital (HOMO) [68, 69]. This difference is called the band gap (E_g). Further, quantum chemical calculations by Bredas et al., reported a linear correlation between I_p and E_a , as well as between E_a and reduction potentials (E_r) [69]. All these parameters are related according to Eq. 2 below [68, 70, 71].

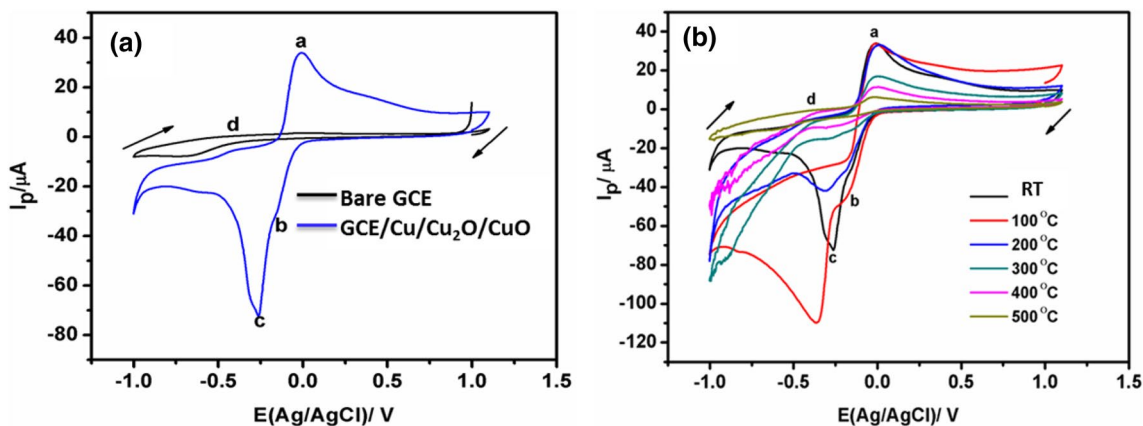


Fig. 6 Typical CVs of **a** bare GCE and GCE/ $Cu/Cu_2O/CuO$ and **b** $Cu/Cu_2O/CuO$ NPs at different annealing temperatures ($0^\circ\text{--}500\text{ }^\circ\text{C}$)

$$\begin{aligned}
 E_a &= (E'_r + 4.4)eV \\
 I_p &= (E'_o + 4.4)eV \\
 E_g &= E_a - I_p
 \end{aligned}
 \tag{2}$$

where E'_r and E'_o are the respective onset reduction and oxidation potentials vs. Ag/AgCl reference electrode [67]. The band gap energy of the Cu/Cu₂O/CuO NPs at different annealing temperatures was calculated to be $E_g = 2.2\text{--}2.5$ eV (at 0–100 °C), $E_g = 2.7\text{--}2.9$ eV (at 200–300 °C) and $E_g = 1.2\text{--}2.4$ eV (at 400–500 °C). The obtained band gap energies are comparable with that of PL measurements. Wang et al. [54] synthesised Cu/Cu₂O NPs using a plant extract and their calculated band gap energies were in agreement with our results.

Following an electrochemical probing of the as-prepared NPs, scan rate dependence studies were carried out to evaluate the adsorption/desorption, diffusion processes and also determine the surface coverage of the Cu/Cu₂O/CuO particles. Figure 7 shows cyclic voltammograms of the Cu/Cu₂O/CuO NPs in 0.2 M PBs, pH 7. The spectra show highly reversible Cu/Cu₂O/CuO NPs at different scan rates. Two distinct redox couples from the pure as-prepared NPs were observed (Fig. 7a) at oxidation peak potential ($E_{p,a}$) = -0.01 V and a reduction peak potential ($E_{p,c}$) = -0.4 V, Fig. 7. The observed peak potentials were attributed to the products of NPs which were associated with redox properties of Cu/Cu₂O/CuO. Nonetheless, a reduction peak current ($I_{p,c}$) at $E_{p,c}$ = -0.4 V was chosen as the peak of interest (Fig. 7(a) b), due to an increase in peak current when Cu/Cu₂O NPs were introduced onto GC electrode surface and since the oxidation peak current showed no trend (Fig. 7(a) a).

From the obtained voltammograms a significant increase in current as a function of scan rate was observed

(Fig. 7b). The increase in current suggests a catalytic effect of the as-prepared NPs. To confirm or facilitate the movement of electrons in the system, the diffusion coefficient (D) and surface coverage (Γ) were calculated using the following equations: For reversible systems, by Randles-Sevcik (Eq. 3) and Laviron equations (Eq. 4) (at 25 °C):

$$I_p = 2.69 \times 10^5 n^3/2 AD^{1/2} v^{1/2} C \tag{3}$$

$$\frac{I_p}{v} = \frac{n^2 F^2 A \Gamma}{4RT} \tag{4}$$

where I_p is the peak current in amperes, v is the scan rate in $V s^{-1}$, the area of an electrode is represented by A in cm^2 , number of electrons transported is represented by n , a diffusional system is presented by D (diffusion coefficient $cm^2 s^{-1}$) and C is the concentration in $mol cm^{-3}$, Γ represents the surface coverage concentration ($mol cm^{-2}$) and F is the Faraday constant. The calculated diffusion coefficient was found to be $1.54 \times 10^{-6} cm^2 s^{-1}$ with the correlation coefficient of (r^2) 0.99. The values were calculated using a reversible equation (Eq. 1). The Laviron equation (Eq. 2) was used to demonstrate the relationship between the current and amount of adsorbed species at a solid surface. The peak current is directly proportional to the surface coverage and the potential scan rate, v [72]. The calculated surface coverage was found to be $1.38 \times 10^{-3} mol cm^{-2}$ for this electrode. The parameter suggests the formation of monolayer at the electrode interface. The scan rate dependence plot of the voltammetric peak currents of Cu/Cu₂O/CuO particles confirmed the behaviour of the system and its response are plotted in Fig. 7a, b. The obtained results suggest a highly catalytic behaviour of the prepared Cu/Cu₂O/CuO NPs whilst possessing capacitance behaviour at

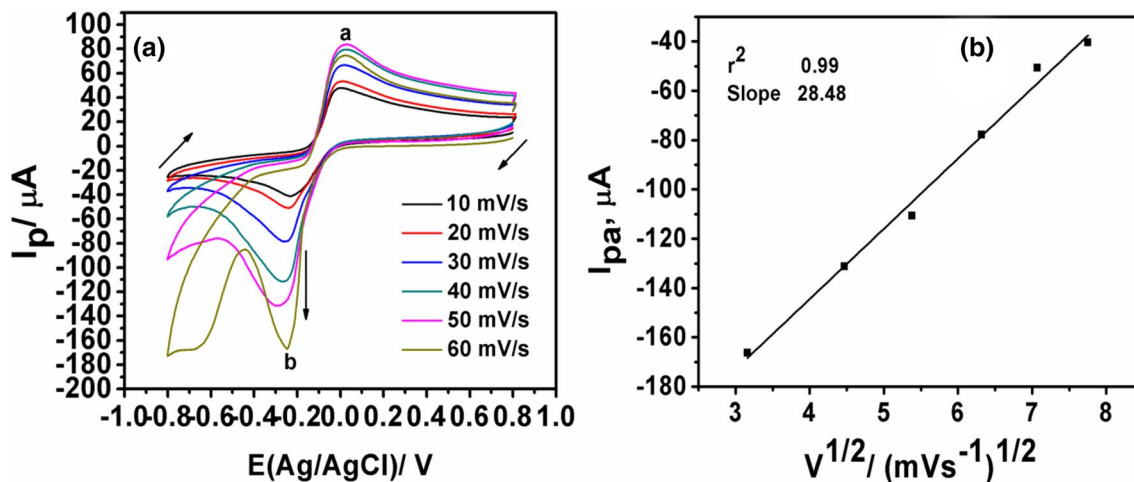


Fig. 7 Typical CVs of Cu/Cu₂O/CuO NPs **a** at different scan rates and **b** a corresponding calibration plot

the oxidation peak potential, apparent by a decrease and increase in peak currents.

Comparative studies between bare and modified GC electrode were evaluated at an applied formal potential of $\Delta E_p = -0.17$ V (observed from CV measurements, Fig. 7) using EIS. The conductivity of the electrodes (GCE and GCE/Cu/Cu₂O/CuO) was characterised using Nyquist plots and bode plots, Fig. 8.

Through fitting and simulation the charge-transfer resistance (R_{ct}) values of bare GC and GC/Cu/Cu₂O electrodes were found to be 432 Ω and 298 Ω , respectively. The results obtained prove that the modified electrodes are more favourable than unmodified electrode, due to lower R_{ct} values. The behaviour in charge transfer resistance suggests a faster electron transfer, thus showing a more conducting system of GCE/Cu/Cu₂O than bare GCE. Some parameters were calculated from the Nyquist plots; the surface coverage (θ) of the modified electrode was calculated to be 1.45×10^{-3} cm s⁻¹ using (Eq. 6). The calculated value is in good agreement with that obtained by CV in which both systems suggest a monolayer at the electrode interface.

$$\theta = 1 - \frac{R_{ct}(Bare/GCE)}{R_{ct}(GCE/Cu/Cu_2O)} \tag{5}$$

Z_r , Z_i —plots, presented in Fig. 8a confirmed that the Cu/Cu₂O/CuO NPs behaves as a typical capacitor over the frequency range of 100 kHz to 0.01 mHz. This behaviour was also confirmed by the presence of some parameters in the equivalent Randles–Sevcik circuit (Insert: Fig. 8a). The parameters as represented in equivalent circuit include; R_s : solution resistance, Z_w : Warburg diffusion impedance, R_{ct} : charge-transfer resistance, and C_f : Faradaic

pseudo-capacitance, respectively. The EIS behaviour was dominated by three phenomena (high, intermediate and low frequency regions) which are denoted by semi-circular mass transfer behaviour which revealed a small polarisation resistance of the nano-oxides film was (high frequency), diffusion of ions at the electrode interface was predominant at the medium frequency and at low frequency, an ideal capacitive behaviour of Cu/Cu₂O/CuO NPs at electrode interface, relative to the bare electrode was obvious. To calculate capacitance and specific capacitance of the NPs, Eq. 4 was used;

$$Z'' = (2\pi fC)^{-1} \tag{6}$$

$$C_{sp} = \frac{-2}{2(\pi mf / |Z''|)} \tag{7}$$

where m represents the mass of an electrode, the frequency is denoted by f and $|Z''|$ is the magnitude of imaginary impedance, C is the capacitance and C_{sp} is the specific capacitance. The capacitance and specific capacitance at -0.17 V calculated from the Z'' values at the high frequency ($f = 100$ kHz) were found to be 11.2 F, 8.76 F and 69–22 F g⁻¹, respectively. The results are in agreement with fitted values. Figure 8b shows the phase angle versus ac frequency relationship for bare GC and GC/Cu/Cu₂O/CuO electrodes. The phase angles and the capacitance of the prepared NPs were observed from bode plot spectra. Theoretically, the capacitor behaves is ideal when $\theta \approx -90^\circ$. However, the phase angles of the prepared NPs are slightly lower by 20° as expected for semiconductor. Conversely, the results reveal the relationship between capacitance vs. frequency. Thus, as the frequency increases, capacitance increases displaying the applicability of the prepared

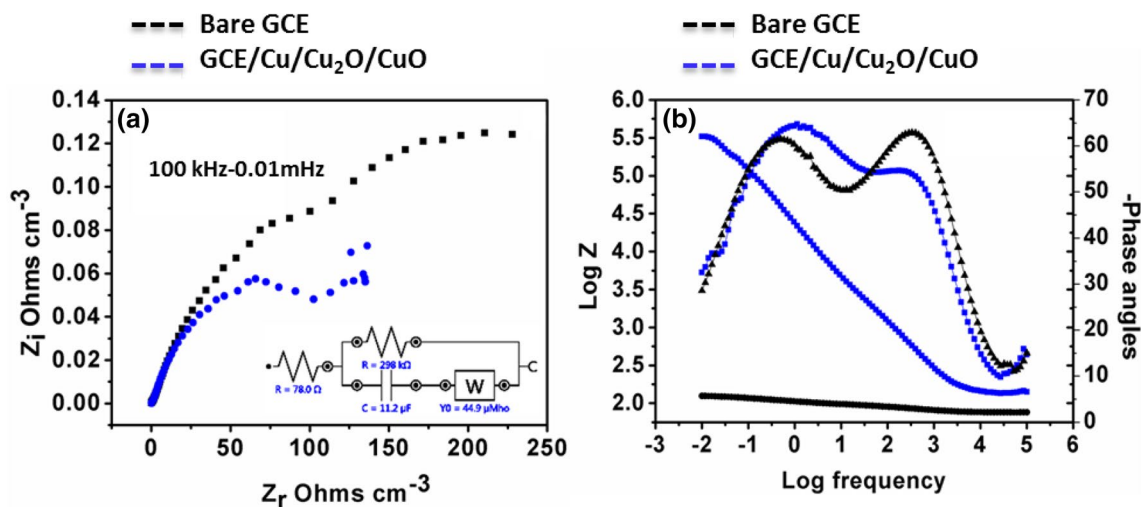


Fig. 8 Typical Nyquist plots of Cu/Cu₂O/CuO NPs (a) and the corresponding bode plots (b)

sample. The results however, prove that with surface modification Cu/Cu₂O/CuO particles can be evaluated as the active material in capacitors applications, evident by the observed experimental and calculated values.

The electrocatalytic activity of as-synthesized Cu/Cu₂O/CuO towards ethanol was investigated with an aqueous solution of 1 M KOH electrolyte using both EIS, Time-based amperometry (i-t), CV and chronocoulometry (CC), Fig. 9a–c. The peak potentials at Fig. 9(a) a-b) are as explained earlier (Figs. 6 and 7).

Compared to bare solution (KOH) Fig. 9(a)(i), Cu/Cu₂O/CuO exhibits fair electrochemical performance for ethanol activity with higher current density and most negative onset potential (OP). The enhancement of catalytic alcohol activity is generally interpreted in terms of the ability to remove intermediates such as CO, which can poison the catalytic surface. It showed a more negative onset potential (-0.3 V), meaning that it requires lower energy for ethanol activity to occur on Cu/Cu₂O. EIS profiles confirmed the kinetics of Cu/Cu₂O at the electrode surface (Fig. 8c). Compared to Fig. 13b(i), Fig. 8b(ii) revealed superior electrical properties towards ethanol. The Randle Sevcik's equivalent circuit (insert, Fig. 8b) was used to assess and simulate the specific parameters as presented by the behaviour of our modified electrodes. Remarkably, the Nyquist plots reveal characteristic small circular curvature Fig. 8b(ii) of

Cu/Cu₂O/CuO at high frequency region signifying that the polarisation resistance (R_p) is prominent, proposing a faster electron shuttling process for ethanol activity. Furthermore, the inclined line at the lower frequency regime denotes a capacitive ($n=0.89$) behaviour and at high frequency, diffusion-controlled system is apparent. The EIS profiles results are consistent with fitted values, CV, and literature data [73, 74]. The relationship between the polarisation resistances and the ethanol concentrations were observed. An apparent decrease in R_p (Fig. 8c: insert) was obvious and suggests an effective electrode as the electrode system was subjected to high concentrations of ethanol. Figure 9d shows the characterisation of ethanol detection using a Cu/Cu₂O/CuO based electrode system. The electrode was immersed a solution containing 1 M KOH as an electrolyte. The electrode was brought to equilibrium by keeping it at -0.017 V (vs. Ag/AgCl electrode (3 M KCl)) and steady-state current (i) was recorded before introduction of ethanol. Different concentrations of ethanol were added to the cell from stock solution and the system was stirred during detection for currents (i_b) response obtained at -0.017 V. The current values ($\Delta i = i_b - i_a$) were plotted against the ethanol concentration in order to determine the working range of the electrode, Fig. 9f. As seen in Fig. 9f, the response currents at the Cu/Cu₂O/CuO based electrode system are directly proportional to the

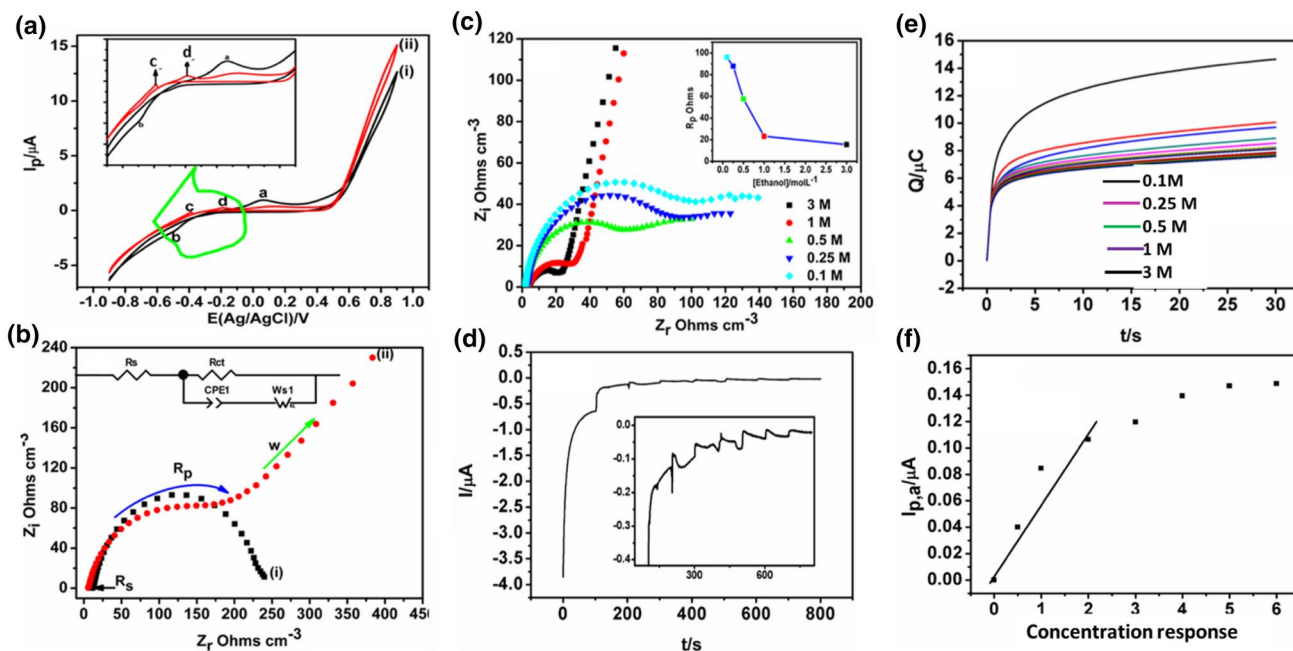


Fig. 9 Shows CV and EIS (a, b) response for ethanol electro-activity by Cu/Cu₂O/CuO modified electrode in alkaline conditions (1 M ethanol + 1 M KOH) at a scan rate of 0.01 Vs⁻¹ vs. Ag/AgCl, c EIS responses of Cu/Cu₂O/CuO modified electrode at different concentrations of ethanol, d Time-based amperometric response of Cu/

Cu₂O/CuO modified electrode at different concentrations of ethanol, e CC response of Cu/Cu₂O/CuO modified electrode at different concentrations of ethanol and f corresponding calibration curve in '(d)'

concentration of ethanol in the range of 0.5–2 μM with a correlation coefficient (r^2) of 0.94 ($n = 6$). From the slope of $0.049 \mu\text{A} \mu\text{M}^{-1}$, the lower limit of detection was estimated to be $0.09 \mu\text{M}$ at a signal to noise ratio of 3. The system further indicates that the response is under the diffusion control at steady state which agrees well with CC (Fig. 9e) and is comparable with other systems such [74]. The amperometric response with long time test for the Cu/Cu₂O/CuO based electrode system was studied under continuous 5 M ethanol flow and no obvious decrease is observed in 400 s, indicating the good stability of the Cu/Cu₂O/CuO based electrode system.

4 Conclusion

In the present work, we report an eco-friendly and cost effect method for the synthesis of Cu/Cu₂O/CuO NPs using peel extract of pomegranate as both capping reducing agent. To the best of our knowledge, a first-time facile strategy to prepare ternary Cu/Cu₂O/CuO NPs and Cu/Cu₂O/CuO structured electrodes. The green synthesised Cu/Cu₂O/CuO nanocrystals were successfully characterised by different techniques and methods. The CV and EIS results coupled with XRD, SEM, FTIR and UV–Vis explored the formation, conductivity, optical and redox processes of Cu/Cu₂O/CuO NPs in neutral media. XRD and SEM revealed the structure and crystalline nature of the NPs with particles size 5–25 nm. FTIR and EDS confirmed the formation of the pure synthesised Cu/Cu₂O/CuO NPs, evident by presence of both Cu–O components. The conductivity nature and the capacitance behaviour of the synthesised Cu/Cu₂O/CuO NPs were exposed by CV, UV–Vis and EIS. Due to high current density (15 j. mA cm^{-2}), $R_p = 20 \Omega$ (capacitive, $n = 0.89$) and $\theta = 70^\circ$, Cu/Cu₂O/CuO electrode proved to be catalytically active towards ethanol using CV and EIS methods. Conclusively, the results suggest that the nanomaterials can be manipulated and controlled at different annealing temperatures to ascertain different morphology. It is noteworthy, that the Cu/Cu₂O/CuO nanoparticles can be evaluated as the active material in capacitors and catalysis applications such as oxygen reduction reaction (ORR) and ethanol oxidation reaction (EOR). The system also proved to be highly sensitive toward ethanol detection.

Acknowledgements The authors are thankful to the Council for Scientific and Industrial Research (CSIR) and National Research Foundation of South Africa (NRF) for funding. We acknowledge the support extended by iThemba Labs and the Department of Materials Division (MRD) for providing us with state-of-the-art facilities and instrumentation.

Author contribution XF: is the main author of the manuscript thus he run experimental work, data interpretation and drafting the

manuscript, MM: helped with the conceptualization, reviewed and edited the manuscript, MM: assisted with electrochemical data interpretation and reviewed the manuscript. All Authors have approved the final manuscript.

Compliance with ethical standards

Conflict of interest The authors declare that they have no competing interests.

References

1. Makarov VV, Sinitsyna OV, Makarova SS, Yaminsky IV, Taliansky ME (2014) Green nanotechnologies: synthesis of metal nanoparticles using plants. *Acta Naturae* 6:35
2. Mehrdad KF (2010) Utilization of fruit waste as biogas plant feed and its superiority. *Turk J Eng Environ Sci* 34:281–287
3. Joshi GG (2013) Microwave assisted organic synthesis: a green chemical approach. *Asian J Pharmaceut Res Dev* 1:165–177
4. Yogamoorthi JA (2014) Green nanobiotechnology: factors affecting synthesis and characterization techniques. *Int J Nanomater Biostruct* 4:66–714
5. Amrut S, Lanje S, Pode B, Ningthoujam S (2010) Optical studies of metal oxide nanofibers. *Adv Appl Sci Res* 1:36–40
6. Abboud Y, Chagraoui A, Bouari EL, Brouzi K, Tanane O, Ihsane B (2014) Biosynthesis, characterization and antimicrobial activity of copper oxide nanoparticles (CONPs) produced using brown alga extract (*Bifurcaria bifurcata*). *Appl Nanosci* 4:571–576
7. Broaddus E, Scott A (2013) Electrochemical characterization of platinum nanotubules made via template wetting nanofabrication. *Int J Electrochem* 2013:7, Article ID 960513. <https://doi.org/10.1155/2013/960513>
8. Zhao C (2012) Preparation of platinum nanoparticles-graphene modified electrode and selective determination of rutin. *Int J Electrochem* 2012:6, Article ID 431253. <https://doi.org/10.4061/2012/431253>
9. Singh RP (2011) Prospects of nanobiomaterials for biosensing. *Int J Electrochem* 2011: 30, Article ID 125487. <https://doi.org/10.4061/2011/125487>
10. Honary S, Fathabad EG, Naghibi F (2012) Green synthesis of copper oxide nanoparticles using microorganism. *Dig J Nanomater Biostruct* 7:999–1005
11. Pasupuleti VR, Shiekh RA, Balam SK, Narasimhulu G, Reddy CS, Rahman IA, Gan SH (2013) Biogenic silver nanoparticles using *Rhinacanthus nasutus* leaf extract: synthesis, spectral analysis, and antimicrobial studies. *Int J Nanomed* 8:3355–3364
12. Akhtar MS, Yun YS (2013) Biogenic synthesis of metallic nanoparticles by plant extracts. *ACS Sustain Chem Eng* 1:591–602
13. Rajan R, Chandran K, Harper SL, Yun SI, Kalaichelvan PT (2015) Green synthesis of silver nanoparticles in aloe vera plant extract prepared by a hydrothermal method and their synergistic antibacterial activity. *Ind Crops Prod* 70:356–373
14. Sana SS, Badineni VR, Arla SK, Boya VK (2015) Eco-friendly synthesis of silver nanoparticles using leaf extract of *Grewia flavescens* and study of their antimicrobial activity. *Mater Lett* 145:347–350
15. Naikaa HR, Manjunathb K, Kumarc D, Nagarajuc G, Sureshde D, Nagabhushana H (2015) Quantitative structure–activity relationship studies of dibenzo[a, d]cycloalkenimine derivatives for non-competitive antagonists of N-methyl-D-aspartate based on density functional theory with electronic and topological descriptors. *J Taibah Univ Sci* 9:7–12

16. Torresdey LG, Gornez E, Videa J, Troiani HE, Santiagol P (2002) Formation and growth of Au nanoparticles inside live alfalfa plants. *Nano Lett* 2:397–401
17. Torresdey LG, Gornez E, Videa J, Troiani HE, Yacaman M (2003) Alfalfa sprouts: a Natural source for the synthesis of silver nanoparticles. *Langmuir* 19:1357–1361
18. Yip SK (1992) Nonlinear Meissner effect in CuO superconductors. *Phys Rev Lett* 69:2264–2267
19. Yadav JA, Nagabhushana H, Basavaraj RB, Lingaraju K, Rajanaika H (2015) Green synthesis, characterization and antibacterial activity of CuO nano particle. *Mater Sci Forum* 830:549–552
20. Kim SJ, Lee CY, Lee JH (2008) CuO nanowire gas sensors for air quality control in automotive cabin. *Sens Actuators B* 135:298–303
21. Umar RA, Al-Hajry A, Hahn YB (2009) Enzymatic glucose biosensor based on flower-shaped copper oxide nanostructures composed of thin nanosheets. *Electrochem Commun* 11:278–281
22. Yang S, Chen L, Chen S (2010) Flower-like CuO hierarchical nanostructures. *Mater Chem Phys* 120:296–301
23. Jiang T, Wang Y, Meng D, Chen J (2014) Controllable fabrication of CuO nanostructure by hydrothermal method and its properties. *Appl Surf Sci* 311:602–608
24. Wang Y, Jiang T, Meng D, Chen J, Hun J (2014) Effect of deposition time on the photoelectrochemical properties of cupric oxide thin films synthesized via electrodeposition method. *Appl Surf Sci* 317:414–421
25. Mikami K, Kido Y, Akaishi Y, Quitain A, Kida T (2019) Synthesis of Cu₂O/CuO nanocrystals and their application to H₂S sensing. *Sensors* 19:211
26. Gawande MB, Goswami A, Zboril R, Varma RS (2016) Cu and Cu-based nanoparticles: synthesis and applications in catalysis. *Chem Rev* 116:3722–3811
27. Hou L, Zhang C, Chen W (2018) CO gas sensors based on p-type CuO nanotubes and CuO nanocubes: morphology and surface structure effects on the sensing performance. *Talanta* 188:41–49
28. Zhang Q, Zhang K, Xu D, Yang S (2014) CuO nanostructures: synthesis, characterization, growth. *Prog Mater Sci* 60:208–237
29. Debbichi LL, Pierson JF, Krüger P (2012) Vibrational properties of CuO and Cu₄O₃ from first-principles calculations, and Raman and infrared spectroscopy. *J Phys Chem C* 116:10232–10237
30. Sahai A (2016) Cu/Cu₂O/CuO nanoparticles: novel synthesis by exploding wire technique and extensive characterization. *Appl Surf Sci* 390:974–983
31. Abd-Elkader OH, Deraz NM (2013) Synthesis and characterization of new copper based nano-composite. *Int J Electrochem Sci* 8:8614–8622
32. Wang Z, Niu Z (2019) Enhancing the ethynylation performance of CuO-Bi₂O₃ nanocatalysts by tuning Cu-Bi interactions and phase structures. *Catalysts* 9:35. <https://doi.org/10.3390/catal9010035>
33. Carnes CL, Klabunde KJ (2002) Synthesis, characterization, and adsorption studies of nanocrystalline copper oxide and nickel oxide. *Langmuir* 18:1352–1359
34. Xu C, Xu G, Wang G (2002) Preparation and characterization of CuO nanorods by thermal decomposition of CuC₂O₄ precursor. *Mater Res Bull* 37:2365–2372
35. Yang G, Zhousheng Y (2012) Electrocatalytic oxidation of hydrogen peroxide based on the shuttlelike nano-CuO-modified electrode. *Int J Electrochem* 2012: 6, article ID194183. <https://doi.org/10.1155/2012/194183>
36. Jnaneshwara DM, Prasad B, Nagabhushana BM, Nagabhushana H, Sharma SC, Chakradha PS (2014) Magnetic and dielectric interactions in nano zinc ferrite powder: prepared by self-sustainable propellant chemistry technique. *J Magn Magn Mater* 339:40–45
37. Fuku XG, Iftikhar FJ, Hess EH, Baker PGL, Iwuoha EI (2012) Cytochrome c biosensor for determination of trace levels of cyanide and arsenic compounds. *Analytica Chimica Acta* 730:49–59
38. Fuku X, Ajayi R, Jijana A, Baker P, Dempsey E, Iwuoha E (2015) Gallium telluride quantum dots bioelectrode system for human epidermal growth factor receptor-2 (Her2/neu) oncogene signalling. *Anal Methods* 7:6114–6124
39. Gunalan S, Venckatesh R (2012) Aloe barbadensis Miller mediated green synthesis of mono-disperse copper oxide nanoparticles: optical properties. *Spectrochim Acta Part A Mol Biomol Spectrosc* 97:1140–1144
40. El-Trass A, El-Mehasseb I, El-Kemary M (2012) CuO nanoparticles: synthesis, characterization, optical properties and interaction with amino acids. *Appl Surf Sci* 258:2997–3001
41. Swarnkar RK (2009) Synthesis of copper/copper-oxide nanoparticles: optical and structural characterizations. *Int J Electrochem* 2009: 7, article ID 11147. <https://doi.org/10.1063/1.3183432>
42. Ren Y, Ma Z, Bruce PG (2012) Transformation of mesoporous Cu/Cu₂O into porous Cu₂O nanowires in ethano. *CrystEngComm* 14:2617–2620
43. Vidyasagar CC, Naik YA, Venkatesha TG, Viswanatha R (2012) Solid-state synthesis and effect of temperature on optical properties of CuO nanoparticles. *Nano-Micro Lett* 4:73–77
44. Tiago U (2005) Self-assembly and selected area growth of zinc oxide nanorods on any surface promoted by an aluminum precoat. *J Phys Chem B* 109:15317–15321
45. Dagher S, Ayeshe A, Tit N (2014) Synthesis and optical properties of colloidal CuO nanoparticles. *J Lumin* 151:149–154
46. Bhattacharjee A, Ahmaruzzaman M (2015) Green Synthesis of 2D CuO nanoleaves (NLs) and its application for the reduction of p-nitrophenol. *Mater Lett* 161:79–82
47. Sharma JK, Srivastava P, Singh G, Akhtar MS, Ameen S (2015) Synthesis, characterization, and adsorption studies of nanocrystalline copper oxide and nickel oxide. *Thermochim Acta* 614:110–115
48. Kumari L, Li WZ (2010) Synthesis, structure and optical properties of zinc oxide hexagonal micropillars. *Cryst Res Technol* 45:311–315
49. Radhakrishnan A (2014) Structural and optical absorption analysis of CuO nanoparticles. *Indian J Adv Chem Sci* 2:158–161
50. Xu F, Shen ZX, Li WS, Tang SH, Ye XR, Jia DZ, Xin XQ (1999) Characterization of CuZnO diodes prepared by ultrasonic spray method. *J Raman Spectrosc* 30:413–415
51. Wang J, Li Z, Jing X, Zhang M, Jiang Z (2009) Synthesis, characterization and structural transformation of a condensed rare earth metal coordination polymer. *J Chem Sci* 121:1077
52. Hoa ND, Jung H, Kim D, Kim H, Hong S (2010) Synthesis of porous CuO nanowires and its application to hydrogen detection. *Sens Actuators B Chem* 146:266–272
53. Debbichi L, Marco de Lucas MC (2012) vibrational Properties of CuO and Cu₄O₃ from first-principles calculations, and raman and infrared spectroscopy. *J Phys Chem Lett C* 116:10232–10237
54. Wang J, Li Z, Jing X, Jiang M (2009) Well-aligned arrays of CuO nanoplatelets. *J Chem Sci* 121:1077–1081
55. Rashad M, Berth G, Lischka K, Pawlis A (2013) CuO and Co₃O₄ nanoparticles: synthesis, characterizations, and Raman spectroscopy. *J Nanomater* 2013: 6, Article ID 714853. <https://doi.org/10.1155/2013/714853>
56. Mageshwari K (2013) Flower-shaped CuO nanostructures: synthesis, characterization and antimicrobial activity. *J Mater Sci Technol* 29:909–914
57. Sathyamoorthy R, Mageshwari K (2013) Facile synthesis of Zn doped CuO hierarchical nanostructures: structural, optical and antibacterial properties. *Physica E* 47:157–161

58. Sutradhar P, Maiti D (2014) Microwave synthesis of copper oxide nanoparticles using tea leaf and coffee powder extracts and its antibacterial activity. *J Nanostruct Chem* 4:86
59. Ananth A, Dharaneedharan S, Heo MS, Mok YS (2015) Copper oxide nanomaterials: synthesis, characterization and structure-specific antibacterial performance. *Chem Eng J* 262:179–188
60. Etefagh R, Azhir E, Shahtahmasebi N (2013) Synthesis of CuO nanoparticles and fabrication of nanostructural layer biosensors for detecting *Aspergillus niger* fungi. *Scientia Iranica* 20:1055–1058
61. Fuku X, Matinise N, Maaza M (2016) Punicalagin green functionalized Cu/Cu₂O/ZnO/CuO nanocomposite for potential electrochemical transducer and catalyst. *Nanoscale Res Lett* 11:356
62. Fuku X (2019) Single step synthesis of bio-inspired NiO/C as Pd support catalyst for dual application: alkaline direct ethanol fuel cell and CO₂ electro-reduction. *J Colloid Interface Sci* 545:138–152
63. Volanti DP, Cavalcante LS, Simoes AZ, Joya MR, Pizani PS, Souza AG (2008) Synthesis and characterization of CuO flower-nanostructure processing by a domestic hydrothermal microwave. *Alloys Compd* 459:537–542
64. Priya SB (2012) Porous palladium nanoflowers that have enhanced methanol electro-oxidation activity. *J Solid State Electrochem* 16:1527–1535
65. Shahrokhian S, Ghalkhani M, Amini MK (2015) Synthesis and biomedical applications of copper oxide nanoparticles. *Electroanalysis* 27:1989–1997
66. Teo WZ, Pumera M (2013) Direct electrochemistry of copper oxide nanoparticles in alkaline media. *Electrochem Commun* 28:51–53
67. Admassie S, Inganäs O, Mammo W, Perzon E, Andersson MR (2006) Electrochemical and optical studies of the band gaps of alternating polyfluorene copolymers. *Synth Met* 156:614–623
68. Erol K, Jürgen R, Thomas N (2003) Determination of quantum confinement in CdSe nanocrystals by cyclic voltammetry. *J Chem Phys* 19:2333–2337
69. Bredas JL, Silbey R, Boudreaux DS, Chance RR (1983) Chain-length dependence of electronic and electrochemical properties of conjugated systems: polyacetylene, polyphenylene, polythiophene, and polypyrrole. *J Am Chem Soc* 105:6555–6559
70. Jennings JC, Albee LD, Kolwyck DC, Surber JB, Taylor ML, Hartnell GF, Lirette RP, Glenn KC (2003) Environmental impact of genetically modified crops. *Poult Sci* 82:371–380
71. Zhang R, Jin GD, Chen D, Hu XY (2009) Arginine, electropolymerized carbon nanotube paste electrode as sensitive and selective, sensor for electrochemical determination of vanillin. *Sens Actuators B Chem* 138:174–181
72. Othman MR, Salimon J (2007) Electrooxidation of glycerol on nickel and nickel alloy. *Malays J Anal Sci* 11:379–387
73. Chtaini A, Abdelmajid SL (2015) Hydrothermal synthesis and hydrogen sensing properties of nanostructured with different morphologies. *Mater Sci Indian J* 12:152–155
74. Wang H, Chi Y, Gao X, Yan X (2017) Progress and challenges in electrochemical sensing of volatile organic compounds using metal-organic frameworks. *J Chem* 2017, Article ID 2346895

Publisher's Note Springer Nature remains neutral with regard to jurisdictional claims in published maps and institutional affiliations.